Materials Today Chemistry 37 (2024) 102024

Contents lists available at ScienceDirect

Materials Today Chemistry

journal homepage: www.journals.elsevier.com/materials-today-chemistry/

Wearable strain sensor utilizing the synergistic effect of $Ti_3C_2T_x$ MXene/AgNW nanohybrid for point-of-care respiratory monitoring

Amit Kumar [a,1], R.K. Rakesh Kumar [b,c,1], Muhammad Omar Shaikh [e], Jia-Yu Yang [a], Aditya Manu Bharti [a], Bo-Yan Huang [a], Hsu-Liang Chang [f], Da-Huei Lee [g], Cheng-Hsin Chuang [a,d,*]

[a] Institute of Medical Science and Technology, National Sun Yat-sen University, Kaohsiung, 80424, Taiwan
[b] Department of Chemical Engineering, National Taiwan University, Taipei City, 10617, Taiwan
[c] Institute of Biomedical Engineering and Nanomedicine, National Healthcare Research Institutes, Miaoli County, 350, Taiwan
[d] Center of Excellence for Metabolic Associated Fatty Liver Disease (CEMAFLD), National Sun Yat-sen University, Kaohsiung, 80424, Taiwan
[e] Sustainability Science and Engineering Program, Tunghai University, Taichung, 407224, Taiwan
[f] Department of Internal Medicine, Kaohsiung Municipal Ta-Tung Hospital, Kaohsiung Medical University Hospital, Kaohsiung Medical University, Kaohsiung, Taiwan
[g] Department of Electrical Engineering, National Chung-Kung University, Tainan, Taiwan

ARTICLE INFO

Keywords:
Wearable
Nanohybrid
Point-of-care
Breath monitoring
Pulmonary function analysis

ABSTRACT

Respiratory signals are significant indicators for detecting changes in physiological conditions and early diagnosis of numerous respiratory illnesses. Herein, we have integrated a high-performance strain sensor and portable circuit board (PCB) with personalized interface to develop point-of-care respiratory monitoring device. The ultrasensitive strain sensor utilizes a conductive polymeric nanocomposite that harnesses the synergistic effect of $Ti_3C_2T_x$ (MXene)/AgNW nanohybrid to develop a wearable device. The wearable device is capable of analysing pulmonary volumes, such as forced volume capacity (FVC) and forced expiratory volume (FEV_1), while accurately recognizing various breathing patterns in a resting state (such as normal, forced, and obstructive), as well as during different physical activities. It shows excellent correlation (>93%) with commercial spirometer for measurement of pulmonary parameters. In addition, we present a wireless device for lab rat respiratory monitoring in anaesthetic state. The device is implemented for real-time respiratory monitoring under mild, normal and high anaesthesia doses. The levels of anaesthesia doses including a critical limit can be significantly discriminated by means of breathing frequency and amplitude, which ultimately results in saving their lives. These results demonstrate the practical feasibility of the strain sensing device as wearable electronics for point-of-care respiratory monitoring in humans and other species.

1. Introduction

The demand for personalized, flexible, and wearable electronics for physiological monitoring has steadily increased, serving the purpose of health monitoring and early detection of various diseases [1–9]. Respiration, as one of the vital markers, is extensively employed to monitor human health and provides a wealth of physiological data that can indicate potential diseases [10–12]. Real-time breath monitoring holds immense potential in detecting these diseases at an early stage, potentially saving lives [13,14]. However, currently utilized respiratory monitoring devices have limited practicality for real-time point-of-care respiratory monitoring due to their uncomfortable fit, complex configurations, and bulky nature [15–17]. Therefore, the need for wearable smart sensors capable of real-time breath monitoring is paramount.

Polymeric nanocomposite-based flexible strain sensors have gained widespread adoption in the development of wearable and flexible devices. This is achieved by incorporating conductive fillers into soft polymers, offering advantages such as cost efficiency, user comfort, and design flexibility. These sensors can effectively monitor various body motions and human respiration by detecting changes in resistance corresponding to strain [18]. Notably, the strain generated by breathing is extremely subtle, making ultra-sensitivity a top priority for fabricating a

* Corresponding author. Institute of Medical Science and Technology, National Sun Yat-sen University, Kaohsiung, 80424, Taiwan.
E-mail address: chchuang@imst.nsysu.edu.tw (C.-H. Chuang).
[1] A.K. and R.K.R.K. have equally contributed to the work.

https://doi.org/10.1016/j.mtchem.2024.102024
Received 9 January 2024; Received in revised form 9 March 2024; Accepted 22 March 2024
Available online 4 April 2024
2468-5194/© 2024 Elsevier Ltd. All rights reserved.

real-time breath monitoring device. In the past, various metallic [19–24] and carbon nanomaterials [25–29] have been used to design various types of sensors, including strain based physical sensors. However, the conventional approach of using a single type of conductive filler limits the overall elastic properties, conductivity, and sensitivity of the nanocomposites. On the other hand, hybrid nanocomposites have demonstrated significant improvements in strain sensing properties through the synergistic effects of the percolative network formed by 1D and 2D nanomaterials within the composite structure [30–34].

In this study, we have prepared a nanohybrid conductive ink by combining AgNWs and MXene through a mixing and centrifuging process, resulting in a hybrid percolative network for the development of an ultrasensitive strain sensor. Unlike traditional strain sensors, this hybrid nanocomposite takes advantage of its unique percolative network to detect even the slightest strains, up to 1%, and represents them as changes in resistance [4]. This level of sensitivity is crucial for designing a real-time breath monitoring device, as breathing induces very minor strains during both expiration and inspiration. To achieve this, the sensor is integrated with straps to create a belt structure, which can be positioned optimally to monitor various breathing patterns during rest (such as normal, forced, and obstructive breathing) as well as different activities. Subsequently, a wireless portable circuit board (PCB) is employed to develop a wearable device for real-time breath monitoring. This device is capable of analysing various lung function parameters, including forced volume capacity (FVC) and forced expiratory volume (FEV_1) in volumetric form, enabling early detection of various pulmonary diseases. Essentially, the device functions as a smart spirometer. Furthermore, we have also implemented the wireless breath monitoring sensor on lab rats to enable real-time respiratory monitoring under mild, normal, and high anaesthesia doses. The device demonstrates significant discrimination between different anaesthesia levels based on breathing frequency and amplitude. Since lab rats are often anesthetized during research, our wireless sensor can provide critical health information, detect potential risks of death, and inform researchers about the well-being of the mice during the anaesthesia process. Overall, this developed system holds immense promise in the field of wearable electronics for personal medical devices, as it enables real-time breath monitoring, early diagnosis of pulmonary diseases, and continuous respiratory monitoring.

2. Experimental methods

• Materials and characterization

Silver nitrate ($AgNO_3$, >99%), N, *N*-Dimethylformamide (DMF, 99.8% anhydrous), calcium chloride ($CaCl_2.H_20$), lithium fluoride (LiF, M_w 25.94), ethylene glycol (EG, anhydrous >99.8%), hydrochloric acid (HCl), poly-vinylpyrrolidone (PVP, M_w 1300 k, 99%), were purchased from sigma Aldrich, thermoplastic polyurethane (TPU, 1175A) was purchased from Taiwan plastics and polymers Taoyuan, Taiwan and Ti_3AlC_2 powder was purchased from Mustec Corp. Hsinchu, Taiwan. Isoflurane (inhalant, Animal Medical no. 08547) was purchased from Baoling Fujin Biotechnology Co., Ltd., Taoyuan, Taiwan.

The surface and structural morphology of the hybrid ink and AgNW-MXene nanocomposite was studied using field emission scanning electron microscopy (FESEM, JEOL-6330) and (HRTEM, JEOL JEM-3010) respectively. Moreover, selected area electron diffraction (SAED) and elemental mapping based compositional analysis of the hybrid ink were performed using energy dispersive X-ray analysis (EDS, X-MAXT).

The physical and mechanical properties of the developed sensor were analysed using an automatic vertical tensile test machine (JSV-H1000). The sheet resistance of the sensing layer was determined using a Four-point probe (Tonghui TH2512+). To measure the resistance after sensor fabrication and the relative change in resistance, a highly sensitive electrometer (KEITHLEY 6514) and a portable circuit board (PCB) were utilized for point-of-care device testing. For comparison and investigation of the sensor output in pulmonary function measurements, a commercially available spirometer (COSMED, REF(C09061-01-99), (SN – 2021074134)) with a USB connection was used. To control the anaesthesia dose concentration for the rat, an isoflurane vaporizer (Matrx VIP 3000) was employed.

• AgNW synthesis

The synthesis procedure for ultralong AgNWs using modified one -pot polyol method has been discussed in detail, previously [35]. Briefly, $AgNO_3$ (0.5 g), PVP (0.75 g) and $CaCl_2$ (0.12 M, 1.1 mL) were homogeneously dispersed in 50 ml of EG to prepare the growth solution. Further, the growth solution was heated for 90 min at 170 °C to prepare ultralong AgNWs of high aspect ratio (>1000). Finally, the synthesized AgNWs were centrifuged with Acetone and ethanol.

• MXene synthesis

Two-dimensional $Ti_3C_2T_x$ MXene was synthesized in bulk by selective etching and delamination from Ti_3AlC_2 using HCl/LiF etchants in acidic solution. Briefly, 4 g of LiF and 4 g of Ti_3AlC_2 were dispersed in HCl (40 ml, 9 mol/L) at 38 °C with continuous stirring. The mixture was kept for 30 h to completely etch the Al atoms and subsequently centrifuged with DI until pH value of ~6.0 for supernatant is achieved. Later, MXene solution was sonicated for 30 min and centrifuged again to attain a homogeneous solution.

• Hybrid nanocomposite synthesis

A nanohybrid based conductive ink utilizing the synergistic effect of percolated AgNW-MXene network was prepared in order to synthesize a highly conductive nanocomposite. Primarily, the synthesized AgNWs (100 ml, 1 wt%) was mixed with varying amounts of MXene (sample A = 0.25 g, sample B = 0.5 g, sample C = 0.75 g and sample D = 1.00 g) and centrifuged with ethanol 2 times and finally with DMF to prepare four different nanohybrid ink as illustrated in Fig. 1a. Later, these nanohybrid conductive inks with percolative properties was mixed with TPU (1.5 g) using DMF (6.5 mL) in a planetary centrifugal mixer to obtain homogeneous nanocomposites.

• Strain sensor fabrication

The four different AgNW-MXene-TPU nanocomposite inks containing fixed AgNW concentrations and varying MXene concentration was spin-coated onto a Teflon substrate and cured in an ambient environment. The sheet resistance of the sensing layer was analysed using a four-point probe machine to investigate its electrical properties. The individual sensing layers were then laser-cut into a rectangular shape measuring 3.5 cm × 1 cm, forming the basis of four different strain sensors. Additionally, the Gauge factor (GF) for these four sensors at 30% strain were investigated to determine optimal fabrication parameters to ensure superior piezoresistive property and overall sensor performance.

To examine the mechanical and electrical properties, double-sided copper tapes were attached to both ends of the sensing layer as electrodes. These electrodes facilitated the connection of wires and allowed for the assessment of the sensor's performance, which will be discussed in a later section. For enhanced sensitivity in detecting minor strains, such as those involved in breath monitoring, slurping, drinking, and pulmonary functions, a belt structure was chosen to develop the strain sensing device. Two flexible and non-elastic individual straps were attached to the ends of the fabricated sensor, creating a belt-like structure. Both straps possess adhesive properties that enable them to adhere to each other and the human body, making it easy to customize the belt's length for different applications. A schematic illustration of the sensor design and its sensing mechanism is presented in Fig. 1b and c

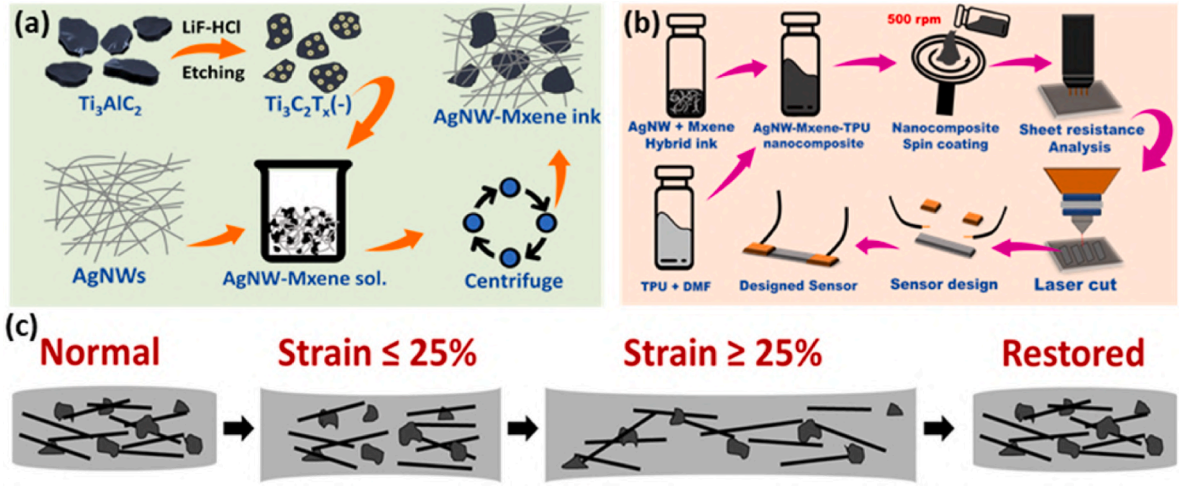

Fig. 1. A schematic for (a) AgNW-MXene nanohybrid ink synthesis protocol, (b) nanocomposite synthesis and sensor fabrication process and (c) its strain-sensing mechanism.

respectively.

3. Results and discussion

The synthesized MXene and AgNWs were individually characterized using HRTEM (High-Resolution Transmission Electron Microscopy) to examine their structural morphology and uniformity. Fig. 2a shows a TEM image of the as-synthesized $Ti_3C_2T_x$ (MXene), while Fig. 2b displays its high-resolution image revealing the Moiré superlattice effect with a d-spacing of 1.22 nm, indicating the presence of few layers. The interplanar distance of the synthesized MXene was further examined, as shown in Fig. 2c–d, to explore the lattice structure. The structural uniformity of the ultralong AgNWs, with a diameter of approximately 40 nm and a very high aspect ratio (>1000), can be observed in Fig. 2e. These individual nanomaterials were then physically mixed using a centrifuging machine to prepare a nanohybrid conductive ink with an embedded percolation network. Fig. 2f and g depict SEM and TEM images of the conductive ink at higher and lower concentrations, respectively, demonstrating that the percolative properties of the conductive ink are preserved and independent of the nanohybrid concentration variation.

To illustrate the presence of both types of individual crystalline nanomaterials in the nanohybrid ink, a Selected Area Electron Diffraction (SAED) pattern is shown in Fig. 2h. The green and red coloured dots represent the lattice points attributed to AgNWs and MXene, respectively. Furthermore, HRTEM-based elemental mapping was performed to explore the elemental composition of the nanohybrid ink. Fig. 2i presents the High-Angle Annular Dark-Field (HAADF) imaging of the nanohybrid ink, while Fig. 2(j–n) show the corresponding elemental mapping for Ti, O, C, Ag, and a merged Energy-Dispersive X-ray Spectroscopy (EDS) layer. Finally, the nanohybrid ink was mixed with TPU (Thermoplastic Polyurethane) to prepare an ultrasensitive polymeric nanocomposite. Fig. 2o and p displays high-resolution SEM images of the prepared AgNW-MXene nanocomposite sensing layer in both normal and cross-section views, demonstrating the preserved percolation network in the three-dimensional polymeric nanocomposite. The nanohybrid-based percolative network results in high sensitivity of the sensor, as the stretching of the sensor leads to a reduction in electrical pathways. The detailed sensing mechanism is given in the supplementary section. Additionally, low-magnification SEM images of the nanocomposite layer in both the normal state and at 100% stretch are presented in Fig. 2q and r, respectively, to explain the sensing mechanism.

To investigate the mechanical properties of the nanocomposite sensor, various tensile tests were conducted to assess its strength, softness, and stability. An automatic vertical force gauge was employed to examine the stress-strain curve, and the corresponding sensor response in the strain range of 20%–100% is depicted in Fig. 3a. It can be observed that the hysteresis is minimal for strains below 40%, which is within the required range for strain sensing in various applications, including our work. However, as the strain range increases, the hysteresis also increases, which can be attributed to the properties of the nanocomposite. In addition, repetitive cycles at 80% strain were performed to evaluate the stability and repeatability of the material. The stress-strain curve and peak force for these tests are shown in Fig. 3b and c, respectively. It is noteworthy that there is minimal change in the peak force during the initial cycles, which becomes saturated in later stages, indicating good stability.

Furthermore, the sensor was vertically stretched at a constant speed of 15 mm/min until it reached its elastic limit. The corresponding output demonstrated that the fabricated sensor can stretch more than 350%, as illustrated in Fig. 3d. Optical images of the sensor in its normal state and at 350% stretch are presented in Fig. 3e and f, respectively, further showcasing its elastic properties. Additional tests, such as load bearing, step resistance, and stability in laundering solutions, were conducted to assess the strength, stability, and compatibility of the nanocomposite sensing layer for wearable sensor applications. The material's stability against sharp objects and laundering solution (tested for 35 h) is demonstrated in Figs. S1 and 3g. Moreover, the sensing layer exhibited an impressive load bearing capacity of 25,000 times its own weight as shown in Fig. 3h–j. With such remarkable mechanical properties, the AgNW-MXene nanocomposite strain sensor shows great potential as a wearable smart sensor.

The challenge of simultaneously achieving high stretchability and conductivity in nanocomposites for wearable devices was addressed through several tests to evaluate the electrical and piezoresistive properties of the strain sensor. Firstly, the sheet resistance of the spin-coated sensing layer was analysed using a four-point probe, as shown in Fig. 4a. It can be concluded that a highly stretchable and conductive nanocomposite sensing layer was synthesized using the synergistic effect of 1D-2D nanomaterial ink. To assess the uniaxial strain sensing properties, the sensor was placed on a horizontal platform. The relative change in resistance ($\Delta R/R$) corresponding to the applied strain (strain%) was measured to evaluate the sensitivity of the sensor, which is also known as gauge factor (GF). Fig. 4b demonstrates variable GFs of 14.4, 30.3, and 73.2 for different strain ranges (0–24%, 24%–38%, and 38%–50%, respectively), highlighting the sensor's ability to detect minor and major strains of the human body. The increase in GF from 14.4 to 73.2 with

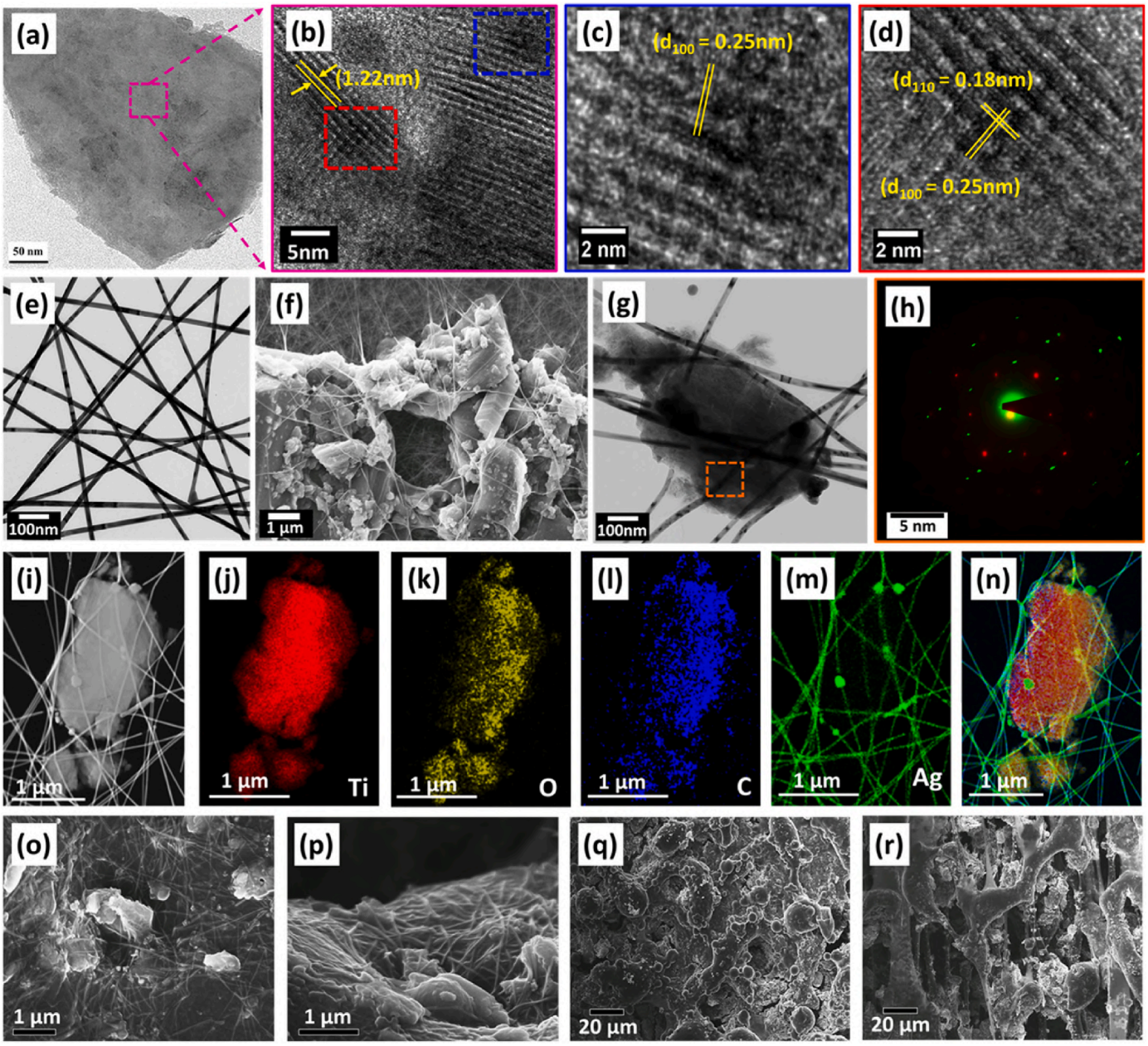

Fig. 2. Nanomaterial Characterization TEM image of synthesized (a) Ti_3C_2 MXene (scale bar 50 nm) (b) observed Moiré's effect in HRTEM image of MXene (scale bar 5 nm) and (c–d) its magnified images to analyse d-spacing; (e) TEM image of AgNWs (scale bar 100 nm); (f) SEM (scale bar 1 µm) and (g) TEM image (scale bar 100 nm) of synthesized AgNW-MXene based hybrid conductive ink with percolation network; (h) SAED pattern of the hybrid ink, where green and red dots represents AgNW and MXene crystal-lattice points respectively (scale bar 5 nm); HRTEM image of Ti_3C_2 MXene HRTEM elemental mapping of hybrid ink displaying (i) HAADF image (scale bar 1 µm), (j–n) Elemental map showing Ti, O, C, Ag and merged EDS layers (scale bar 1 µm); High-resolution SEM image of (o) AgNW-MXene nanocomposite (scale bar 1 µm) and (p) its cross-section view (scale bar 1 µm); SEM image of AgNW-MXene nanocomposite in (q) normal state (scale bar 20 µm) and (r) and stretched state (scale bar 20 µm). (For interpretation of the references to colour in this figure legend, the reader is referred to the Web version of this article.)

increasing strain is attributed to the detachment of multiple current pathways formed by MXene. The strain sensing properties were also analysed with variation in stretching frequency, as shown in Fig. 4c. The frequency was increased from 0.5 Hz to 5 Hz at 10% strain, and the sensor exhibited negligible changes in ΔR/R with varying stretching frequency, as depicted in Fig. 4d. Repeatability tests were conducted to ensure accurate strain sensing in lower and higher strain ranges, as demonstrated in Fig. 4e and f, respectively. The ultrasensitive nature of the sensor was demonstrated through an LED intensity test, as shown in supporting Video S1. The sensor was stretched from the normal state to 20%, 50%, and 100%, and the corresponding changes in LED intensity were shown in Fig. 4g–j in the same order. The decrease in LED light intensity corresponds to a reduction in conductive pathways in the percolation network, resulting in an increase in sensor resistance. Finally, the sensor's durability was assessed through a repeatability test of more than 30,000 cycles at 10% strain to ensure its reliable strain sensing properties, as depicted in Fig. 4k. The sensor exhibited negligible changes in ΔR/R over 30,000 cycles, as shown in the enlarged images in Fig. 4k, and ultimately returned to its initial resistance after the test.

Supplementary video related to this article can be found at https://doi.org/10.1016/j.mtchem.2024.102024

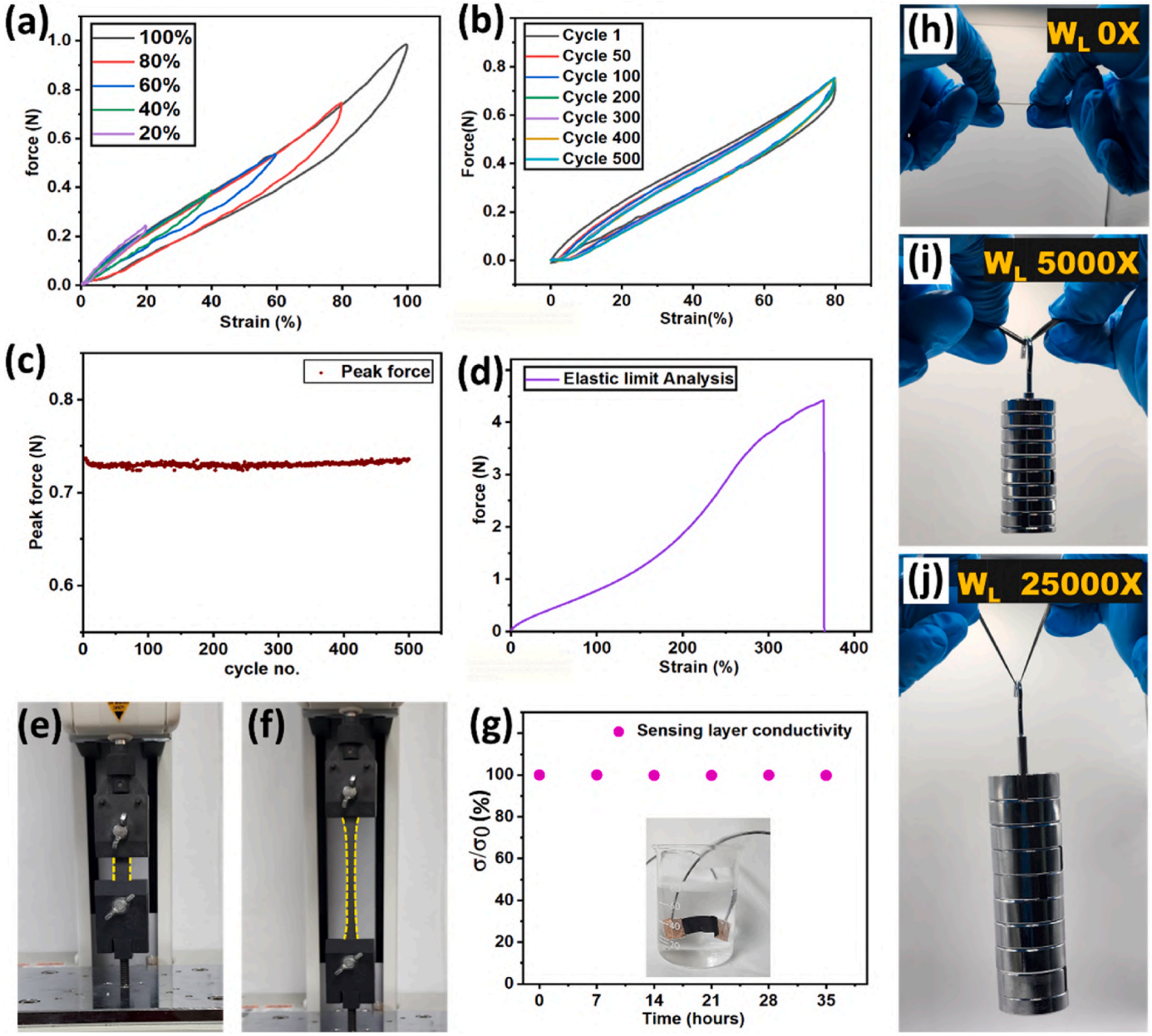

Fig. 3. Mechanical properties analysis: Stress-strain analysis for (a) lower strain (20–100%), (b) repeatability test for 500 cycles (80% strain) and (c) the peak force value for 500 cycles, (d) elastic limit of the sensor; illustration of sensor elastic properties in (e) normal state and (f) stretched (over 350% strain); (g) Sensor stability against detergent solution for 35 h; numerous weights loading such as (h) no load, (i) 5000 times and (j) 25,000 times to depict the mechanical strength of the sensing layer.

The proposed strain sensor, with its high sensitivity, elasticity, wide sensing range, and skin-like properties, can be implemented on the human body for a variety of applications in wearable smart sensors for motion detection. The sensor was patched on various body parts, including biceps, knee, neck, finger, elbow, and wrist, to detect numerous body motions during activities or exercising. The sensor responses for these body motions have been shown in Fig. S2.

To detect minor strains from the body during breathing and swallowing, an ultrasensitive and precise sensor is required. The proposed sensor has a very high-resolution limit (1% strain), which is necessary for real-time breath monitoring and pulmonary function analysis [36–38]. The sensor was attached with two inelastic adhesive straps to design a patchable belt for accurate real-time breath monitoring. A portable circuit board with a mini battery transmits the data wirelessly as depicted in Fig. 5a. Fig. 5b shows the block diagram of the signal processing function for the strain sensing using the PCB interface. A resistive readout circuit converts the resistance change from the belt structured strain sensor to be a voltage difference. The small voltage difference from the resistive readout circuit is amplified by the programmable gain amplifier (PGA) in the micro-controller unit (MCU). Furthermore, the analog-to-digital converter (ADC) in the MCU transforms the analog voltage signal to the digital data streams. The digital data is processed through micro-processing logic and later wirelessly transmitted through the Bluetooth module. To develop a point-of-care respiratory monitoring device, the wireless portable circuit board (PCB) with a high frequency (1–10 Hz) of data acquisition was internally connected to the belt for wireless transmission of the sensor output as shown in Fig. 5c. The device was fastened on the human body to examine its practical applicability for real-time breath monitoring, as illustrated in Fig. 5d. A volunteer was asked to sit normally in a resting

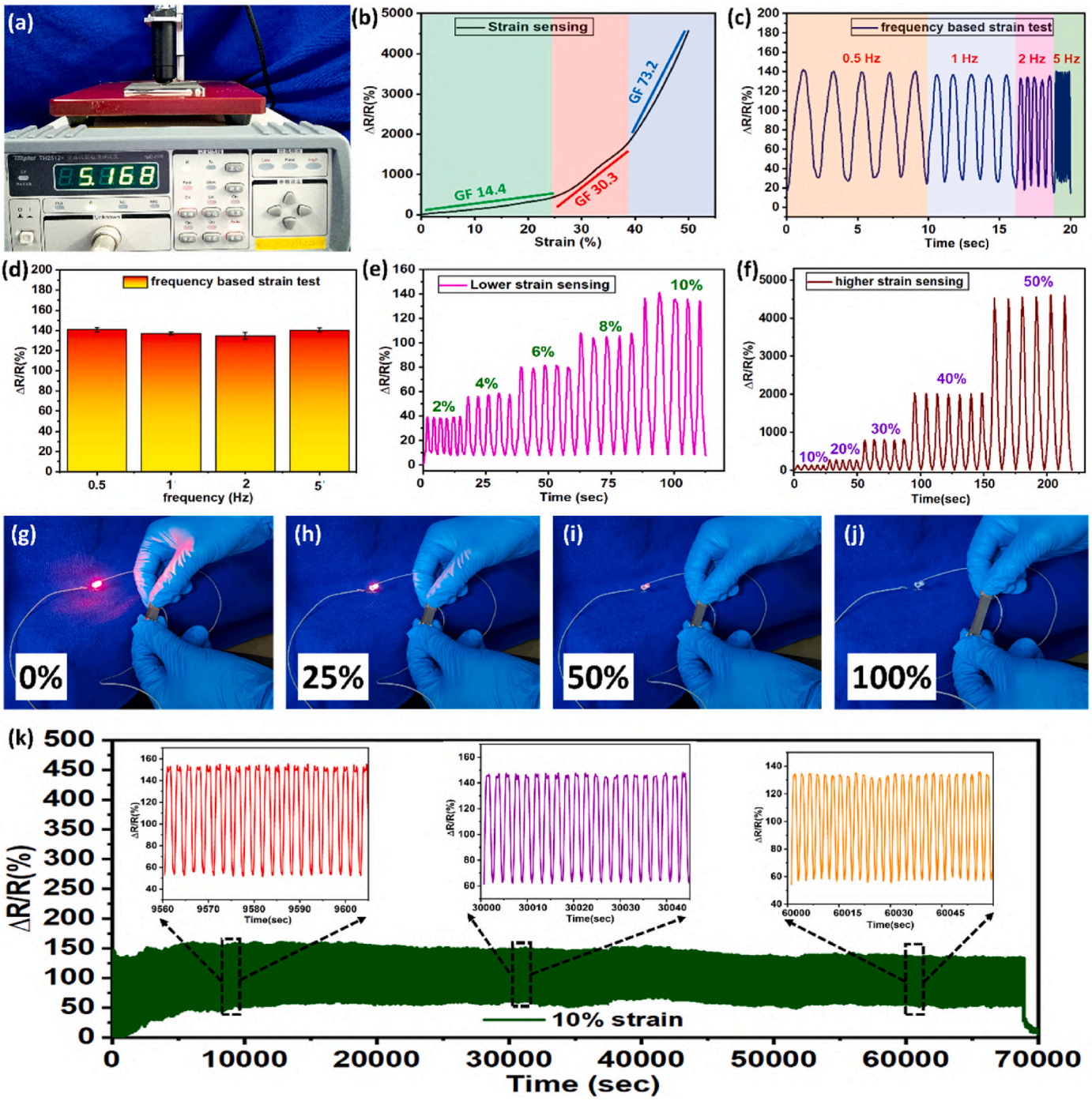

Fig. 4. Piezoresistive properties analysis (a) sheet resistance measurement of nanocomposite sensing layer using four point probe; (b) strain sensing property of the fabricated sensor; (c–d) frequency dependent strain sensing properties of the sensor; (e) lower and (f) higher strain sensing properties of the sensor; LED intensity test demonstrating the high sensitivity of fabricated sensor for (g) 0%, (h) 25%, (i) 50% and (j) 100% strains; (k) Sensor repeatability test for 30,000 cycles at 10% strain.

state for real-time breath monitoring, as demonstrated in supplementary Video S2. Fig. 5e shows the device response for various types of breathing, including normal breathing, quick breathing, forced apnea (hold and release), and deep breathing in the resting state. The device accurately distinguishes numerous breathing patterns based on breathing frequency and amplitude. The enlarged images for normal breathing and quick breathing have been shown in Fig. 5f and g, respectively. It has been observed that normal breathing is composed of 15–17 breaths per minute (bpm) with a maximum ΔR/R of 11%, while quick breathing has 20–30 bpm with a maximum ΔR/R of 39%. Deep breathing (Fig. 5i) results in significantly higher ΔR/R with wider breathing peaks and a very low breathing frequency (10–12 bpm). The device can also be utilized to investigate the obstruction in the breathing pattern and sleep apnea, as depicted in Fig. 5h. Obstruction in the breathing pattern leads to a constant ΔR/R value signifying the pause/hold in breathing. Additionally, the device was implemented for real-time breath monitoring during activities such as drinking hot coffee and cycling. The corresponding breathing pattern for slurping is characterized by extended inhalation during slurping, followed by partial exhalation (PE), swallowing of the liquid (S) and complete exhalation (CE) as

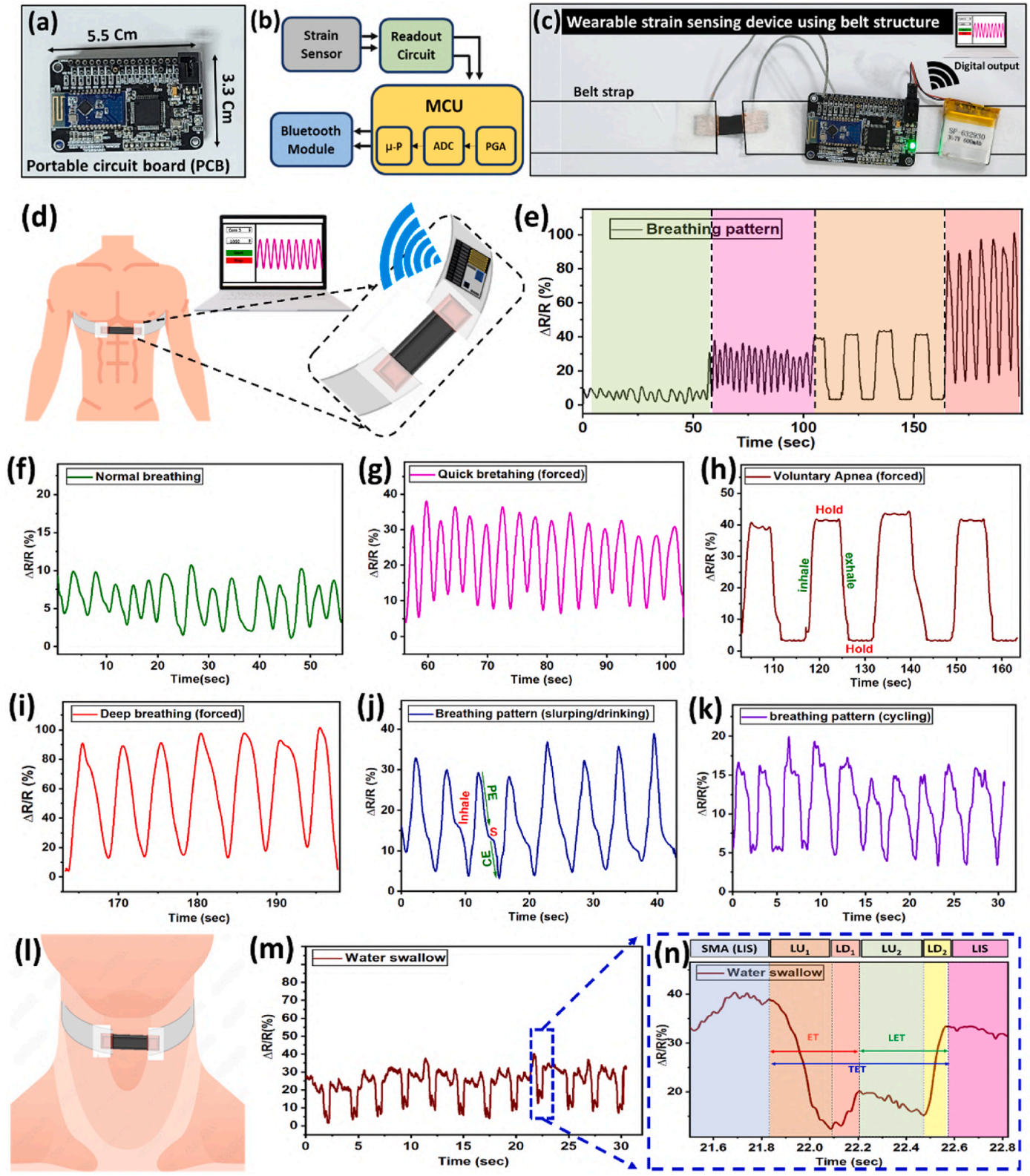

Fig. 5. Real time minor strain testing using wearable device: (a) a portable circuit board and (b) its circuit diagram for signal analysis and transmission (c) An illustration of belt-structured design of wearable respiratory monitoring device. (d) a schematic for breath monitoring analysis using the belt structured strain sensor; (e) relative change in resistance for four different type of breathing such as (f) normal breathing, (g) quick breathing, (h) voluntary apnea and (i) deep breathing; Real time relative change in resistance while (j) slurping hot coffee and (k) cycling; (l) a schematic for water swallowing analysis using the same sensor (m) the corresponding relative change in resistance for water swallowing and (n) its detailed magnified image.

shown in Fig. 5j. It has been noticed that slurping requires inhaling extra air to drink the hot liquid, which results in higher amplitude and simultaneously affects the breathing pattern [39,40]. The breathing frequency (~20 bpm) and corresponding ΔR/R were comparatively increased while cycling (Fig. 5k), which is quite obvious as cycling results in faster breathing, highlighting the practical feasibility of the device for point-of-care breath monitoring. Moreover, the device was attached to the neck in a stretched state to accurately analyse the water drinking procedure to decipher swallowing disorder. Fig. 5l and supporting Video S3 demonstrate the experimental setup for this analysis. The corresponding response for multiple water swallowing cycles is shown in Fig. 5m–and a magnified image of one cycle is displayed in Fig. 5n.

Supplementary video related to this article can be found at https://doi.org/10.1016/j.mtchem.2024.102024

The swallowing procedure consists of two stepswherein the suprahyoid muscle activation (SMA) is followed by the upward motion (LU_1) and downward motion (LD_1) of the larynx. During these motions, the sensor experiences compression and stretching, leading to a change in relative resistance. This step, known as excursion time (ET), takes less than 0.4 s. The second step is similar to the first one, involving the upward motion (LU_2) and downward motion (LD_2) of the larynx. However, this step starts before the larynx reaches its initial position and helps in swallowing remnant water [41]. The time taken for this step, known as lateral excursion time (LET), is $\leq$ 0.37 s. The total excursion time (TET), which refers to the duration of time taken by the patient to completely swallow the water and larynx reaches its initial state (LIS), is $\leq$ 0.8 s [42,43]. The detailed analysis of the water swallowing procedure using the

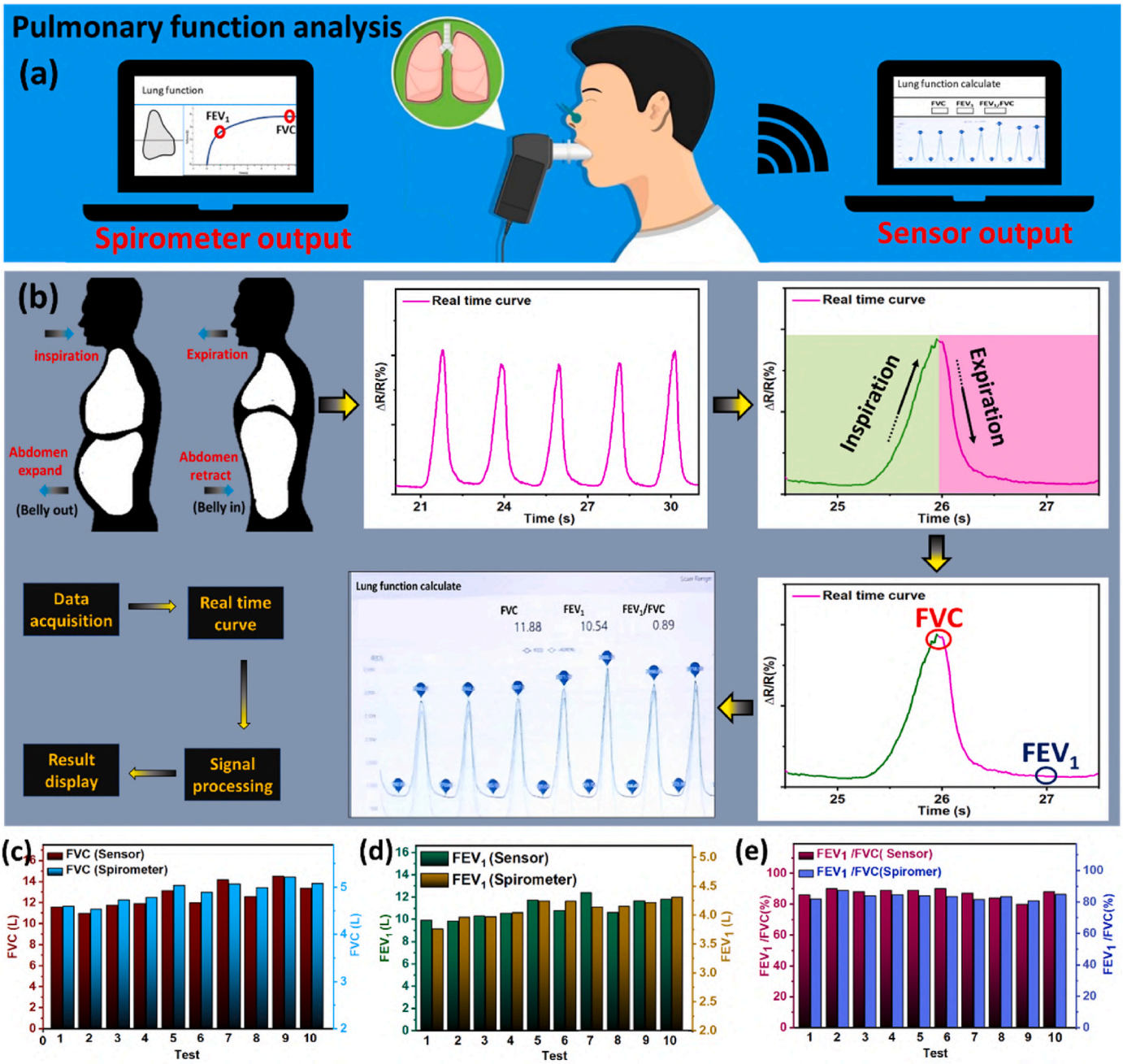

Fig. 6. Pulmonary function analysis and comparison (a) A schematic for the comparison of pulmonary functions using commercially used spirometer and proposed smart spirometer using the strain sensor. (b) schematic diagram of real time data assessment and processing utilizing smart spirometer. Comparison of pulmonary functions parameters such as (c) FVC, (d) FEV_1 and (e) FEV_1/FVC measured by the commercial spirometer and smart spirometer.

device can be further utilized to investigate water swallowing disorders in the near future for the development of a point-of-care device. This device has the potential to provide valuable insights into swallowing disorders and assists in diagnosing and monitoring patients.

Pulmonary function parameters, such as FVC, FEV_1 and their corresponding ratio (FEV_1/FVC), are crucial for analysing respiratory health and detecting respiratory diseases at an early stage. The FVC represents the maximum exhaled volume of air, while the amount of air exhaled within the first second corresponds to FEV_1. The FEV_1/FVC ratio is used to assess the healthiness of the respiratory system in humans [44,45]. Currently, spirometers used in hospitals are rigid, have complex configurations, and are not wearable. However, nanocomposite-based wearable strain sensors offer promise for breath monitoring due to their comfortability and skin-like features. In this study, a portable circuit board (PCB) is attached to the strain sensor to design a smart and wearable spirometer for real-time breath monitoring and pulmonary function analysis. The smart spirometer can be attached to the abdominis muscle for real-time pulmonary function analysis [36,37]. Fig. 6a illustrates the schematic for simultaneous pulmonary function analysis using the smart spirometer and a commercial spirometer. The smart spirometer utilizes the strain sensing properties of the sensor during expiration and inspiration to provide a real-time $\Delta R/R$ curve. Signal processing is then used to identify the inspiration and expiration cycles. The maximum $\Delta R/R$ helps assess the FVC value, while the change in $\Delta R/R$ after 1 s assists in evaluating the FEV_1 value, as previously reported and shown in Fig. S3 [24]. Fig. 6b presents a schematic for data acquisition in real-time, signal processing, and the observed results using the smart spirometer. Several tests have been conducted to compare the pulmonary function measurements obtained from the smart spirometer and the commercial spirometer simultaneously. Fig. 6c shows the FVC values measured by both spirometers, while Fig. 6d displays the FEV_1 values. Strong correlations between the measurements of the smart spirometer and the commercial spirometer for FVC and FEV_1 can be observed (refer to Figs. S4 and S5, respectively). Additionally, the FEV_1/FVC ratio has been evaluated by both spirometers (Fig. 6e), and their correlation is presented in Fig. S6.

It is important to note that the smart spirometer can be easily worn under clothing and used for continuous monitoring of pulmonary function in real-time (refer to video S4), whereas commercially used spirometers lack this feature. The smart spirometer, with advantages such as continuous real-time monitoring, wearing comfortability, and cost-efficiency, demonstrates the true potential of wearable devices for respiratory monitoring.

Supplementary video related to this article can be found at https://doi.org/10.1016/j.mtchem.2024.102024

The laboratory mouse has become a valuable animal model in various areas of biomedical research [46]. During biomedical tests, mice are often anesthetized to ensure stable conditions for conducting experiments [47,48]. Therefore, continuous respiration monitoring is crucial to ensure the health and stability of the animals during these procedures. The fabricated sensor with the belt structure can be used for long-term continuous breath monitoring of laboratory rats while they are anesthetized, as shown in Fig. 7a–c. The setup for the anaesthesia process and breath monitoring is illustrated in Fig. 7a. Initially, the mouse is anesthetized using an isoflurane vaporizer controller in an anaesthesia chamber. After the anaesthesia induction, the mouse is transferred to the breath monitoring platform, where the breathing pattern is analysed using the belt structure, as shown in Fig. 7b. The belt is fastened around the chest or abdomen of the mouse, as depicted in Fig. 7c. The relative change in resistance of the sensor is then analysed using a wireless portable circuit board designed to transmit the digital output. The anaesthesia dose can lead to changes in blood oxygenation, which, in turn, affects the breathing pattern of the mice [49,50]. To analyse the breathing pattern in detail, various anaesthesia doses with different concentrations have been tested and compared. These include mild doses (0.5% concentration), normal doses (2% concentration), and high doses (4% concentration) of anaesthesia. The relative change in resistance signals obtained by monitoring respiration during mild dose, normal dose, and high dose anaesthesia is shown in Fig. 7d, e, and 7f, respectively. These signals represent the breathing patterns of the mice under different anaesthesia concentrations. A significant difference in the breathing patterns can be observed with changes in anaesthesia concentration [51]. The results suggest that the mice's breathing pattern is minimally influenced by a mild dose of anaesthesia (supporting video S5), while significant changes in amplitude and breathing frequency are observed with a normal dose and high dose of anaesthesia [52,53].

Supplementary video related to this article can be found at https://doi.org/10.1016/j.mtchem.2024.102024

To improve the quality of the breathing signals and remove noise, the signals are filtered using specific low-pass FFT filters. The relative change in resistance after noise reduction for mild dose, normal dose, and high dose anaesthesia is shown in Figs. 7g, 6h and 6i, respectively. It is important to note that the filters not only reduce noise but also contribute to assessing the breathing frequency. For mild dose anaesthesia, an average change in relative resistance of 0.61% and a breathing frequency of 1.95 Hz were observed as shown in Fig. 7j. The average change in relative resistance (6%) and breathing frequency (1.3 Hz & 1.4 Hz) for normal dose anaesthesia is displayed in Fig. 7k. At high dose anaesthesia, sharp panting indicates that the dose was intolerable for the mouse. The breathing frequency reduced to 1 Hz, and an average change in relative resistance of 23.4% was observed during breathing (Fig. 7l). To verify the effectiveness of the filtering process, the superimposed signals before and after filtering for different anaesthesia doses are displayed in Figs. S7–9. This comparison confirms the successful noise reduction and improved signal quality achieved through filtering.

A comparison with previously reported breath monitoring sensors (Table S1) and the conducted tests have demonstrated the practical feasibility and promising potential of the proposed device for point-of-care health monitoring. This device is applicable not only to humans but also to animals, particularly laboratory mice. By continuously monitoring the breathing pattern of laboratory mice exposed to different anaesthesia doses, researchers can gain valuable insights into the effects of anaesthesia on the respiratory system. Additionally, the wireless and portable nature of the device enables convenient, non-invasive monitoring, making it invaluable for long-term studies and improving animal welfare during anaesthesia and experiments.

4. Conclusion

A flexible and wearable strain sensor was developed by harnessing the synergistic effects of AgNW-MXene nanohybrid within a polymeric nanocomposite. Owing to its percolative properties, the sensor exhibits high conductivity and exceptional sensitivity, enabling it to detect strains with outstanding precision. The sensor was integrated with a wireless interface within a belt structure, creating a point-of-care device for breath monitoring and pulmonary function analysis. This innovative device is capable of effectively analysing and distinguishing various breathing patterns during rest and different activities, while also assessing pulmonary functions. Real-time analysis of crucial pulmonary parameters such as FVC and FEV is possible with the proposed wireless device, which exhibits a strong correlation (>93%) with commercial devices. Furthermore, the device was successfully employed in anesthetized laboratory rats to study their breathing patterns under different anaesthesia doses. The device enables easy investigation and comparison of anaesthesia dose levels, including the critical dose limit. These results emphasize the practical applicability of the device as a point-of-care tool for respiratory monitoring in both humans and animals.

CRediT authorship contribution statement

Amit Kumar: Writing – original draft, Visualization, Methodology, Investigation, Data curation, Conceptualization. **R.K. Rakesh Kumar:**

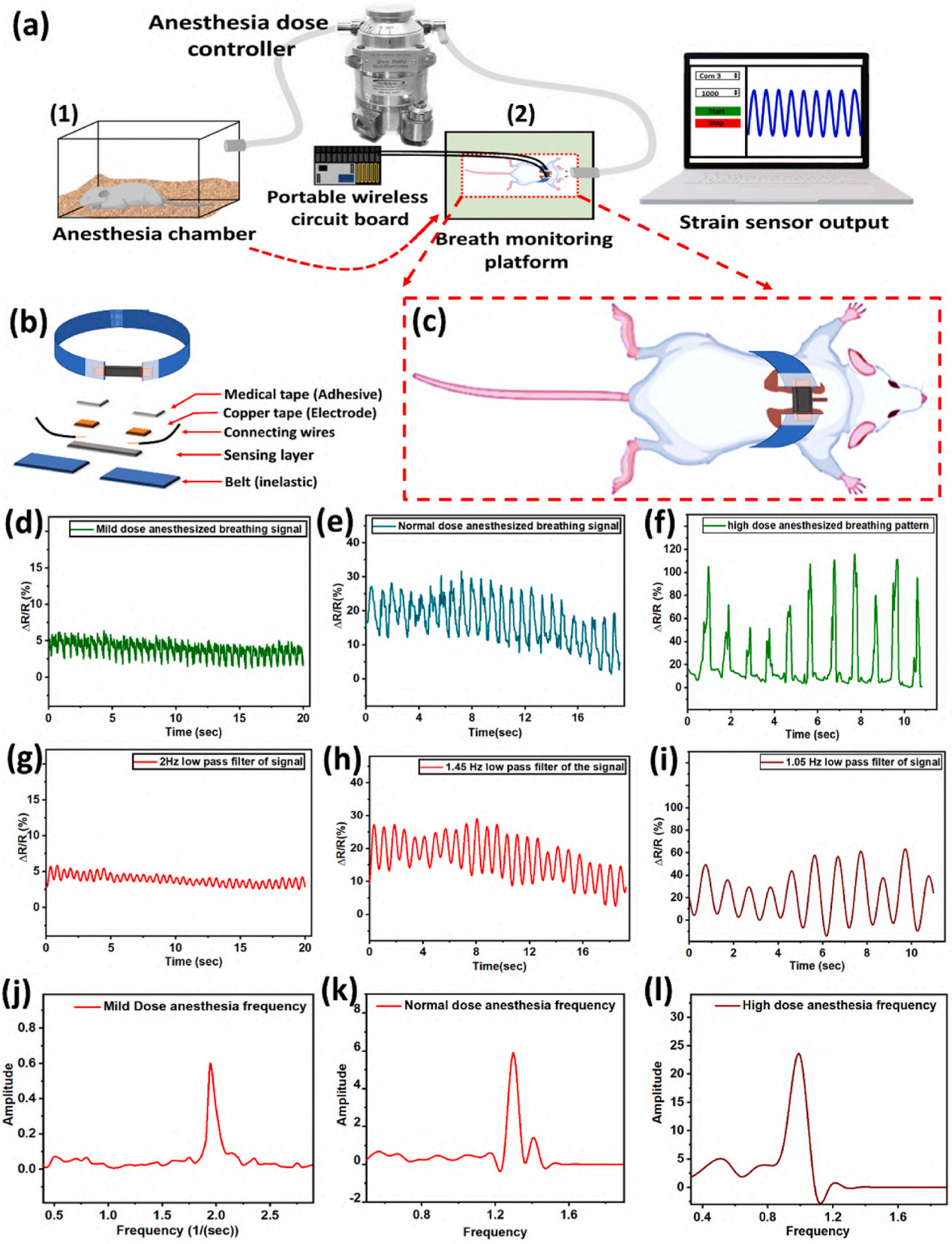

Fig. 7. Anesthetized lab rat breath monitoring analysis A schematic diagram (a) for the mice breath monitoring analysis, (b) of the breath monitoring strain sensor belt and its components used for analysis. (c) Magnified image of mice with the belt on its body; The relative change in resistance due to breathing when the rat is exposed to (d) mild dose, (e) normal dose and (f) high dose anaesthesia along with their corresponding filtered signals at (g) 2 Hz (low pass), (h) 1.45 Hz (low pass), and (i) 1.05 Hz (low pass) frequency respectively. FFT analysis of the output for analysing the breathing frequency and amplitude for (j) mild dose (k) normal dose and (l) high dose anaesthesia.

Writing – original draft, Validation, Investigation. **Muhammad Omar Shaikh:** Writing – review & editing, Validation. **Jia-Yu Yang:** Validation, Investigation. **Aditya Manu Bharti:** Investigation, Data curation. **Bo-Yan Huang:** Software, Investigation. **Hsu-Liang Chang:** Supervision, Resources, Methodology. **Da-Huei Lee:** Software, Data curation. **Cheng-Hsin Chuang:** Writing – review & editing, Validation, Supervision, Funding acquisition, Conceptualization.

Declaration of competing interest

The authors declare the following financial interests/personal relationships which may be considered as potential competing interests:

Cheng-Hsin Chuang reports financial support was provided by National Sun Yat-sen University. If there are other authors, they declare that they have no known competing financial interests or personal relationships that could have appeared to influence the work reported in this paper.

Data availability

Data will be made available on request.

Acknowledgments

The authors would like to thank the Ministry of Science and Technology (MOST) Taiwan, for financially supporting this research under Contract No. MOST 110-2221-E-110-034-MY3. The authors would also like to thank the Centre for Nanoscience and Nanotechnology, Research Center for Metabolic dysfunction Associated Fatty Liver Diseases (MAFLD Center), National Sun Yat-sen University for aiding with the material's characterization.

Appendix A. Supplementary data

Supplementary data to this article can be found online at https://doi.org/10.1016/j.mtchem.2024.102024.

References

[1] T.Q. Trung, N.E. Lee, Flexible and stretchable physical sensor integrated platforms for wearable human-activity monitoringand personal healthcare, Adv. Mater. 28 (22) (2016) 4338–4372.
[2] R.K.R. Kumar, et al., Electrochemical immunosensor utilizing a multifunctional 3D nanocomposite coating with antifouling capability for urinary bladder cancer diagnosis, Sensor. Actuator. B Chem. 384 (2023) 133621.
[3] S. Shen, X. Xiao, J. Chen, Wearable triboelectric nanogenerators for heart rate monitoring, Chem. Commun. 57 (48) (2021) 5871–5879.
[4] A. Kumar, et al., Ultrasensitive strain sensor utilizing a AgF–AgNW hybrid nanocomposite for breath monitoring and pulmonary function analysis, ACS Appl. Mater. Interfaces 14 (50) (2022) 55402–55413.
[5] Y. Ma, et al., Self-powered, one-stop, and multifunctional implantable triboelectric active sensor for real-time biomedical monitoring, Nano Lett. 16 (10) (2016) 6042–6051.
[6] R.R. Kumar, et al., Recent advances and emerging trends in cancer biomarker detection technologies, Ind. Eng. Chem. Res. 62 (14) (2023) 5691–5713.
[7] S. Imani, et al., A wearable chemical–electrophysiological hybrid biosensing system for real-time health and fitness monitoring, Nat. Commun. 7 (1) (2016) 11650.
[8] R.K.R. Kumar, M.O. Shaikh, C.-H. Chuang, A review of recent advances in non-enzymatic electrochemical creatinine biosensing, Anal. Chim. Acta 1183 (2021) 338748.
[9] C.-T. Pan, et al., PVDF/AgNP/MXene composites-based near-field electrospun fiber with enhanced piezoelectric performance for self-powered wearable sensors, Int. J. Bioprint. 9 (1) (2023).
[10] M. Wang, et al., Air-flow-driven triboelectric nanogenerators for self-powered real-time respiratory monitoring, ACS Nano 12 (6) (2018) 6156–6162.
[11] X. Peng, et al., All-nanofiber self-powered skin-interfaced real-time respiratory monitoring system for obstructive sleep apnea-hypopnea syndrome diagnosing, Adv. Funct. Mater. 31 (34) (2021) 2103559.
[12] Y. Su, et al., Self-powered respiration monitoring enabled by a triboelectric nanogenerator, Adv. Mater. 33 (35) (2021) 2101262.
[13] Z. Liu, et al., Expandable microsphere-based triboelectric nanogenerators as ultrasensitive pressure sensors for respiratory and pulse monitoring, Nano Energy 59 (2019) 295–301.
[14] Z. Zhao, et al., Machine-washable textile triboelectric nanogenerators for effective human respiratory monitoring through loom weaving of metallic yarns, Adv. Mater. 28 (46) (2016) 10267–10274.
[15] T. Dinh, et al., Stretchable respiration sensors: Advanced designs and multifunctional platforms for wearable physiological monitoring, Biosens. Bioelectron. 166 (2020) 112460.
[16] Y. Liu, et al., Epidermal electronics for respiration monitoring via thermo-sensitive measuring, Mater. Today Phys. 13 (2020) 100199.
[17] B. Zhang, et al., Breath-based human–machine interaction system using triboelectric nanogenerator, Nano Energy 64 (2019) 103953.
[18] J.-Y. Yang, et al., Biocompatible, Antibacterial, and stable deep eutectic solvent-based ionic gel multimodal sensors for healthcare applications, ACS Appl. Mater. Interfaces 15 (48) (2023) 55244–55257.
[19] A. Kumar, M.O. Shaikh, C.-H. Chuang, Silver nanowire synthesis and strategies for fabricating transparent conducting electrodes, Nanomaterials 11 (3) (2021) 693.
[20] M.D. Ho, et al., Percolating network of ultrathin gold nanowires and silver nanowires toward "invisible" wearable sensors for detecting emotional expression and apexcardiogram, Adv. Funct. Mater. 27 (25) (2017) 1700845.
[21] Y. Huang, et al., Highly stretchable strain sensor based on polyurethane substrate using hydrogen bond-assisted laminated structure for monitoring of tiny human motions, Smart Mater. Struct. 27 (3) (2018) 035013.
[22] P. Khosravi, et al., Deep learning enables robust assessment and selection of human blastocysts after in vitro fertilization, NPJ Digital Med. 2 (1) (2019) 1–9.
[23] R.K. Rakesh Kumar, et al., Zwitterion-functionalized cuprous oxide nanoparticles for highly specific and enzymeless electrochemical creatinine biosensing in human serum, ACS Appl. Nano Mater. 6 (3) (2023) 2083–2094.
[24] Y. Wang, et al., Hierarchically buckled Ti3C2Tx MXene/carbon nanotubes strain sensor with improved linearity, sensitivity, and strain range for soft robotics and epidermal monitoring, Sensor. Actuator. B Chem. 368 (2022) 132228.
[25] L.-Q. Tao, et al., Graphene-paper pressure sensor for detecting human motions, ACS Nano 11 (9) (2017) 8790–8795.
[26] T. Dinh, et al., Environment-friendly carbon nanotube based flexible electronics for noninvasive and wearable healthcare, J. Mater. Chem. C 4 (42) (2016) 10061–10068.
[27] X. Liao, et al., A highly stretchable ZnO@ fiber-based multifunctional nanosensor for strain/temperature/UV detection, Adv. Funct. Mater. 26 (18) (2016) 3074–3081.
[28] A. Yamamoto, et al., Monitoring respiratory rates with a wearable system using a stretchable strain sensor during moderate exercise, Med. Biol. Eng. Comput. 57 (12) (2019) 2741–2756.
[29] R.K.R. Kumar, et al., Enzymeless electrochemical biosensor platform utilizing Cu2O-Au nanohybrids for point-of-care creatinine testing in complex biological fluids, Sensor. Actuator. B Chem. 399 (2024) 134787.
[30] I. Kim, et al., A photonic sintering derived Ag flake/nanoparticle-based highly sensitive stretchable strain sensor for human motion monitoring, Nanoscale 10 (17) (2018) 7890–7897.
[31] J. Liu, et al., Visualized simulation for the nanostructure design of flexible strain sensors: from a numerical model to experimental verification, Mater. Horiz. 6 (9) (2019) 1892–1898.
[32] Y. Yu, et al., Wrinkled nitrile rubber films for stretchable and ultra-sensitive respiration sensors, Extreme Mech. Lett. 11 (2017) 128–136.
[33] L. Lan, et al., Highly conductive 1D-2D composite film for skin-mountable strain sensor and stretchable triboelectric nanogenerator, Nano Energy 62 (2019) 319–328.
[34] Y. Wang, et al., High linearity, low hysteresis Ti3C2Tx MXene/AgNW/liquid metal self-healing strain sensor modulated by dynamic disulfide and hydrogen bonds, Adv. Funct. Mater. 33 (37) (2023) 2301587.
[35] A. Kumar, et al., Highly sensitive, flexible and biocompatible temperature sensor utilizing ultra-long Au@ AgNW-based polymeric nanocomposites, Nanoscale 14 (5) (2022) 1742–1754.
[36] C. Ning, et al., Helical fiber strain sensors based on triboelectric nanogenerators for self-powered human respiratory monitoring, ACS Nano 16 (2) (2022) 2811–2821.
[37] M. Chu, et al., Respiration rate and volume measurements using wearable strain sensors, NPJ Digital Med. 2 (1) (2019) 8.
[38] Z. Liu, et al., A highly sensitive stretchable strain sensor based on multi-functionalized fabric for respiration monitoring and identification, Chem. Eng. J. 426 (2021) 130869.
[39] B. Martin-Harris, et al., Breathing and swallowing dynamics across the adult lifespan, Arch. Otolaryngol. Head Neck Surg. 131 (9) (2005) 762–770.
[40] T. Nishino, T. Yonezawa, Y. Honda, Effects of swallowing on the pattern of continuous respiration in human adults, Am. Rev. Respir. Dis. 132 (6) (1985) 1219–1222.
[41] S. Teramoto, Y. Fukuchi, Detection of aspiration and swallowing disorder in older stroke patients: simple swallowing provocation test versus water swallowing test, Arch. Phys. Med. Rehabil. 81 (11) (2000) 1517–1519.
[42] C.M. Wang, et al., Aging-related changes in swallowing, and in the coordination of swallowing and respiration determined by novel non-invasive measurement techniques, Geriatr. Gerontol. Int. 15 (6) (2015) 736–744.
[43] S. Teramoto, et al., Simple two-step swallowing provocation test for elderly patients with aspiration pneumonia, Lancet 353 (9160) (1999) 1243.
[44] M.P. Swanney, et al., Using the lower limit of normal for the FEV1/FVC ratio reduces the misclassification of airway obstruction, Thorax 63 (12) (2008) 1046–1051.
[45] S.P. Bhatt, et al., Discriminative accuracy of FEV1: FVC thresholds for COPD-related hospitalization and mortality, JAMA 321 (24) (2019) 2438–2447.

[46] P.M.L. Janssen, et al., The need for speed: mice, men, and myocardial kinetic reserve, Circ. Res. 119 (3) (2016) 418–421.
[47] A.J. Ewald, Z. Werb, M. Egeblad, Dynamic, long-term in vivo imaging of tumor–stroma interactions in mouse models of breast cancer using spinning-disk confocal microscopy, Cold Spring Harb. Protoc. 2011 (2) (2011) pdb–top97.
[48] N. Milani-Nejad, P.M.L. Janssen, Small and large animal models in cardiac contraction research: advantages and disadvantages, Pharmacol. Therapeut. 141 (3) (2014) 235–249.
[49] K.L. Navarro, et al., Mouse anesthesia: the art and science, ILAR J. 62 (1–2) (2021) 238–273.
[50] C. Lee, T.A. Jones, Effects of ketamine compared with urethane anesthesia on vestibular sensory evoked potentials and systemic physiology in mice, JAALAS 57 (3) (2018) 268–277.
[51] C.M. Zehendner, H.J. Luhmann, J.-W. Yang, A simple and novel method to monitor breathing and heart rate in awake and urethane-anesthetized newborn rodents, PLoS One 8 (5) (2013) e62628.
[52] S.K. Lemieux, G.H. Glover, An infrared device for monitoring the respiration of small rodents during magnetic resonance imaging, J. Magn. Reson. Imag. 6 (3) (1996) 561–564.
[53] A.J. Ewald, Z. Werb, M. Egeblad, Monitoring of vital signs for long-term survival of mice under anesthesia, Cold Spring Harb. Protoc. 2011 (2) (2011) pdb-prot5563.